CrossMark

NICER X-Ray Observations of Seven Nearby Rotation-powered Millisecond Pulsars

Sebastien Guillot[1,2] , Matthew Kerr[3] , Paul S. Ray[3] , Slavko Bogdanov[4] , Scott Ransom[5] , Julia S. Deneva[6] ,
Zaven Arzoumanian[7], Peter Bult[7], Deepto Chakrabarty[8] , Keith C. Gendreau[7], Wynn C. G. Ho[9,10] , Gaurava K. Jaisawal[11] ,
Christian Malacaria[12,13] , M. Coleman Miller[14] , Tod E. Strohmayer[15] , Michael T. Wolff[3] , Kent S. Wood[16],
Natalie A. Webb[1,2], Lucas Guillemot[17,18] , Ismael Cognard[17,18], and Gilles Theureau[17,18,19]

[1] IRAP, CNRS, 9 avenue du Colonel Roche, BP 44346, F-31028 Toulouse Cedex 4, France; sebastien.guillot@irap.omp.eu
[2] Université de Toulouse, CNES, UPS-OMP, F-31028 Toulouse, France
[3] Space Science Division, Naval Research Laboratory, Washington, DC 20375, USA
[4] Columbia Astrophysics Laboratory, Columbia University, 550 West 120th Street, New York, NY 10027, USA
[5] National Radio Astronomy Observatory, 520 Edgemont Road, Charlottesville, VA 22903, USA
[6] George Mason University, resident at the Naval Research Laboratory, Washington, DC 20375, USA
[7] Astrophysics Science Division, NASA Goddard Space Flight Center, Greenbelt, MD 20771, USA
[8] MIT Kavli Institute for Astrophysics and Space Research, Massachusetts Institute of Technology, 70 Vassar Street, Cambridge, MA 02139, USA
[9] Department of Physics and Astronomy, Haverford College, 370 Lancaster Avenue, Haverford, PA 19041, USA
[10] Mathematical Sciences, Physics and Astronomy, and STAG Research Centre, University of Southampton, Southampton SO17 1BJ, UK
[11] National Space Institute, Technical University of Denmark, Elektrovej 327-328, DK-2800 Lyngby, Denmark
[12] NASA Marshall Space Flight Center, NSSTC, 320 Sparkman Drive, Huntsville, AL 35805, USA
[13] Universities Space Research Association, NSSTC, 320 Sparkman Drive, Huntsville, AL 35805, USA
[14] Department of Astronomy and Joint Space-Science Institute, University of Maryland, College Park, MD 20742, USA
[15] Astrophysics Science Division and Joint Space-Science Institute, NASA Goddard Space Flight Center, Greenbelt, MD 20771, USA
[16] Praxis, resident at the Naval Research Laboratory, Washington, DC 20375, USA
[17] Laboratoire de Physique et Chimie de l'Environnement et de l'Espace, LPC2E, CNRS-Université d'Orléans, F-45071 Orléans, France
[18] Station de Radioastronomie de Nançay, Observatoire de Paris, CNRS/INSU, F-18330 Nançay, France
[19] LUTH, Observatoire de Paris, PSL Research University, CNRS, Université Paris Diderot, Sorbonne Paris Cité, F-92195 Meudon, France

Abstract

The *Neutron star Interior Composition Explorer* observed several rotation-powered millisecond pulsars (MSPs) to search for or confirm the presence of X-ray pulsations. When broad and sine-like, these pulsations may indicate thermal emission from hot polar caps at the magnetic poles on the neutron star surface. We report confident detections ($\geqslant 4.7\sigma$ after background filtering) of X-ray pulsations for five of the seven pulsars in our target sample: PSR J0614−3329, PSR J0636+5129, PSR J0751+1807, PSR J1012+5307, and PSR J2241−5236, while PSR J1552+5437 and PSR J1744−1134 remain undetected. Of those, only PSR J0751+1807 and PSR J1012+5307 had pulsations previously detected at the 1.7σ and almost 3σ confidence levels, respectively, in *XMM-Newton* data. All detected sources exhibit broad sine-like pulses, which are indicative of surface thermal radiation. As such, these MSPs are promising targets for future X-ray observations aimed at constraining the neutron star mass–radius relation and the dense matter equation of state using detailed pulse profile modeling. Furthermore, we find that three of the detected MSPs exhibit a significant phase offset between their X-ray and radio pulses.

Unified Astronomy Thesaurus concepts: Neutron stars (1108); Rotation powered pulsars (1408); Millisecond pulsars (1062); X-ray identification (1817)

1. Introduction

Millisecond pulsars (MSPs) are old neutron stars (NSs; with characteristic ages $\tau \sim 10^9$ yr) named so based on their millisecond-range rotation periods ($P \lesssim 25$ ms), with the fastest known having $P \simeq 1.4$ ms (Hessels et al. 2006). In contrast, the bulk of the pulsar population is observed with spin periods in the ~ 0.1–10 s range. As they age, these pulsars evolve beyond the so-called "pulsar death line" (Sturrock 1971; Hibschman & Arons 2001) where they stop emitting in the radio band. Old pulsars spinning at millisecond periods must have experienced a "recycling" process of spin-up. Pulsar recycling occurs via the transfer of angular momentum due to the accretion of matter from a binary companion onto the NS, during the low-mass X-ray binary phase (Bisnovatyi-Kogan & Komberg 1974; Alpar et al. 1982; Radhakrishnan & Srinivasan 1982). Once this recycling process ends, the magnetic field re-establishes the MSP magnetosphere, enabling the re-activation of the pulsed radio emission. Overall, MSPs are characterized

by their large ages, exceptional rotational stability, and low magnetic fields ($B \sim 10^{8-9}$ G).

While strong evidence exists that low-mass X-ray binaries are the progenitors of MSPs (Wijnands & van der Klis 1998; Papitto et al. 2013), not all MSPs are found in binary systems. This may be because the orbital modulations of MSPs have not yet been discovered (possibly due to faintness, or long orbital periods; e.g., Bassa et al. 2016; Kaplan et al. 2016), or because the NS is truly isolated. Possible explanations invoke the ablation of the companion (as in black-widow and redback systems; Chen et al. 2013) or the disruption of the binary system (via stellar encounters in dense environments). It has also been suggested that some isolated MSPs might have been formed by the direct collapse of a massive white dwarf (Freire & Tauris 2014).

X-ray pulsations in MSPs were first discovered in *ROSAT* observations of PSR J0437−4715 (Becker & Trümper 1993). These apparently thermal pulsations were ascribed to heating of the surface due to internal friction, or due to polar cap heating

caused by magnetospheric return currents along open NS magnetic field lines (Harding & Muslimov 2001, 2002). Since this discovery, the X-ray emission from a handful of MSPs (mostly in globular clusters) has been identified as due to hot $\sim 10^6$ K thermal (blackbody-like) emission from an area that is much smaller than the entire NS surface (e.g., Bogdanov et al. 2006, 2011; Zavlin 2006; Forestell et al. 2014; Lee et al. 2018). These small and hot polar caps at or close to the NS surface generate broad sine-like modulations with large pulsed fraction ($\sim$30%–70%) as the NS rotates. It was realized early on that the X-ray pulse profiles of MSPs could provide probes of the physical properties of NSs (compactness, or mass-to-radius ratio; Pavlov & Zavlin 1997) when modeled with a realistic NS atmosphere (Zavlin et al. 1996). This seminal work prompted detailed studies of the modeling of X-ray pulsations of MSPs (e.g., Bogdanov et al. 2007, 2008; Bogdanov & Grindlay 2009).

Measuring the compactness—and, in the best circumstances, the radius—of an NS is a crucial tool to determine the still-unknown equation of state (EOS) of dense nuclear matter. Obtaining constraints on the NS radius from the modeling of MSP pulse profiles provides a powerful method to discriminate between the numerous theoretical models describing dense nuclear matter (for a recent review, see Lattimer & Prakash 2016). Modeling MSP pulse profiles is a very promising technique that complements alternative methods making use of other classes of thermally emitting NSs (e.g., Heinke et al. 2006, 2014; Webb & Barret 2007; Özel et al. 2010, 2016; Steiner et al. 2010, 2013, 2018; Guillot et al. 2013; Miller 2013, 2016; Bogdanov et al. 2016; Guillot 2016; Baillot d'Etivaux et al. 2019), and methods exploiting the gravitational wave signals from NS–NS mergers as demonstrated with the GW170817 event (e.g., Abbott et al. 2017, 2018; De et al. 2018).

The *Neutron star Interior Composition Explorer* (*NICER*; Gendreau & Arzoumanian 2017) was designed to fully exploit the pulse profile modeling technique, which requires data with high signal-to-noise ratios (S/N), as the main scientific goal of the *NICER* mission is to constrain the radii of NSs from observations of a handful of MSPs. An additional science goal of the mission is to study the X-ray flux modulations of pulsars and discover new sources of X-ray pulsations (Ray et al. 2018). This includes searching for X-ray pulsations from NSs that would be suitable for pulse profile modeling with *NICER* or with future missions (e.g., *STROBE-X*, Ray et al. 2019a; *eXTP*, Watts et al. 2019; or the *Athena X-ray Observatory*, Nandra et al. 2013). Prior to the launch of *NICER*, only four thermally dominated MSPs were known to exhibit highly significant X-ray pulsations: PSR J0437−4715 (Becker & Trümper 1999; Zavlin et al. 2002; Bogdanov 2013), PSR J0030+0451 (Becker & Aschenbach 2002; Bogdanov et al. 2008), PSR J2124−3358 (Becker & Trümper 1999; Zavlin 2006; Bogdanov et al. 2008), and PSR J1024−0719 (Zavlin 2006). A few other MSPs showed tentative or marginal detections: PSR J0751+1807 at 1.7σ and PSR J1012+5307 at almost 3σ (Webb et al. 2004b); and PSR J1614−2230 at the 4σ level (Pancrazi et al. 2012).

Most radio MSPs hosted in globular clusters are found to be positionally coincident with soft, thermal X-ray sources (e.g., Bogdanov et al. 2006, 2011; Forestell et al. 2014), whose spectra suggest that their emission also arises from the heated magnetic polar caps of the NS. A long *Chandra* High Resolution Camera (HRC) observation of 47 Tuc yielded 4σ

pulsation detections for three MSPs hosted by this cluster (Cameron et al. 2007). Some MSPs with nonthermal emission also exhibit pulsations in the X-ray band, although they tend to be characterized by short-duty-cycle pulse profiles with hard nonthermal spectra (e.g., PSR B1821−24 in the globular cluster M28, PSR B1937+21; Gotthelf & Bogdanov 2017; Deneva et al. 2019), likely caused by magnetospheric emission. Others, such as PSR J0218+4232, have a hard nonthermal spectrum with moderately broad X-ray profiles (Webb et al. 2004a; Deneva et al. 2019).

Aside from the thermally emitting MSPs mentioned above, those in globular clusters, and the nonthermal emitters, a number of relatively nearby MSPs show apparently thermal X-ray emission, but were not previously observed in a mode permitting searches for pulsations and/or with sufficient exposures. These include PSR J0023+0923 (a black-widow with a very soft X-ray spectrum; Gentile et al. 2014), PSR J0034−0534 (Zavlin 2006), PSR B1257+12 (the pulsar with planets; Pavlov et al. 2007), PSR J1400−1431 (a very nearby but very X-ray faint MSP; Swiggum et al. 2017), and PSR J1909−3744 (Kargaltsev et al. 2012; Webb et al. 2019). A complete list of X-ray-emitting MSPs in the Galactic field has been compiled by Lee et al. (2018).

No systematic study exists on the offsets between the radio and X-ray pulses of rotation-powered MSPs, in part because of the challenging aspects of properly aligning the pulse profiles. For those MSPs with thermal emission, originating from the footprints of the magnetic field at the NS surface, one naturally expects the X-ray and radio profiles to be aligned. This is indeed observed for a handful of MSPs: PSR J0437−4715 (Bogdanov 2013), PSR J0030+0451 (Bilous et al. 2019), or PSR J1231−1411 (Ray et al. 2019b). However, some exceptions include PSR J1614−2230 (Pancrazi et al. 2012) or PSR J2124−3358 (Becker & Trümper 1999), although for the latter, the 1σ uncertainty is 1 ms, i.e., $\sim$20% of the total spin period. For nonthermal MSPs, for which the emission originates in the magnetosphere, some have been observed with near perfect alignment (PSR B1821−24 or PSR B1937+21; Deneva et al. 2019), possibly suggesting a similar location for the origin of the radio and X-ray emission. Others, however, show a significant offset, such as PSR J0218+4232, in which the broad double-peaked radio pulse lies halfway between the two moderately broad X-ray pulses (Deneva et al. 2019).

A selection of nearby MSPs in the field of the Galaxy with known thermal emission, but no prior firm detection of X-ray pulsations, have been targeted by *NICER* to detect or confirm the presence of polar cap emission causing pulsations. Here we report on the results from these observations and the discovery of pulsations in some of them. Section 2 briefly presents the targets and some of their basic properties. Section 3 describes the observations performed, the data reduction and search method. The results are presented in Section 4 and are followed by a brief discussion on the properties of the detected pulsations and conclusions in Section 5.

2. Targets

For this investigation, we considered MSPs that had no previous securely identified X-ray pulsations. This included targets with only marginal detections of pulsations. The basic properties of these MSPs are summarized in Table 1, and we provide below an overview of some of their characteristics and details about prior X-ray observations. Other MSPs with

Table 1
Selection of Nearby MSPs Targeted by *NICER*

Pulsar	P (ms)	$\dot{P}$ ($\times 10^{-21}$)	$P_{\rm orb}$ (day)	D (pc)	M ($M_\odot$)	Timing Solution
PSR J0614−3329	3.10	17.5	53.6	∼2690	unknown	NRT
PSR J0636+5129	2.87	3.38	0.066	203^{+27}_{-21}	unknown	NRT
PSR J0740+6620	2.88	12.2	4.77	400^{+200}_{-100}	$2.17^{+0.11}_{-0.10}$	(1)
PSR J0751+1807	3.48	7.79	0.25	1070^{+240}_{-170}	1.64 ± 0.15	NRT
PSR J1012+5307	5.26	17.1	0.6	907 ± 131	1.83 ± 0.11	NRT
PSR J1231−1411	3.68	22.8	1.86	∼420	unknown	(2)
PSR J1552+5437	2.43	2.80	...	∼2600	⋯	*Fermi*/LOFAR
PSR J1614−2230	3.15	9.624	8.7	670^{+50}_{-40}	1.908 ± 0.016	(1)
PSR J1744−1134	4.08	8.935	...	440^{+20}_{-20}	⋯	NRT
PSR J2241−5236	2.19	6.64	0.15	∼960	unknown	Parkes

Notes. Distances with quoted uncertainties are based on measurements of parallax from radio timing. For the rest, a dispersion measure (DM)-based distance estimate is given (Yao et al. 2017). The $\dot{P}$ value reported are not corrected for the Shklovskii effect. "NRT" stands for the *Nançay Radio Telescope*.
[a] *NICER* observations presented in Z. Arzoumanian et al. (2019, in preparation).
[b] *NICER* observations presented in Ray et al. (2019b).

known pulsations and observed by *NICER* for EoS determination purposes are presented in Bogdanov et al. (2019).

2.1. PSR J0614−3329

The 3.1 ms spin period of PSR J0614−3329 was discovered by the Robert C. Byrd Green Bank Telescope (GBT) from a source detected in γ-rays with the *Fermi* Large Area Telescope (LAT; Ransom et al. 2011) but with no known counterpart at any other wavelength. With a period derivative of $\dot{P} \approx 1.75 \times 10^{-20}$ s s^{-1}, this pulsar's surface dipolar magnetic field is $B \approx 2.38 \times 10^8$ G (Ransom et al. 2011). The orbital period of 53.6 days was also measured from radio timing. The companion star, tentatively a helium white dwarf, was identified from its optical colors in *g*-, *r*-, and *i*-band Gemini observations, despite the pulsar's proximity to a background galaxy (∼10″, Testa et al. 2015). Finally, X-ray data obtained with the *Neil Gehrels Swift Observatory* indicated a likely thermal X-ray spectrum with a blackbody temperature $kT_{\rm BB} = 0.23 \pm 0.05$ keV (Ransom et al. 2011).

2.2. PSR J0636+5129

The Green Bank Northern Celestial Cap (GBNCC) survey for pulsars discovered this 2.87 ms pulsar in a 95.6 minute binary orbit (Stovall et al. 2014). Based on its orbital properties, the system was initially classified as a black-widow binary, although some features typically seen in black-widow pulsars are lacking (e.g., eclipses and dispersion measure variations; Stovall et al. 2014). The binary companion was recently discovered as a magnitude $r \approx 24$ low-mass ($M < 0.02\, M_\odot$) companion star. As no radial velocity information was available, no constraints on the pulsar mass were obtained (Draghis & Romani 2018). *XMM-Newton* data of PSR J0636+5129 showed a thermal spectrum, with $kT_{\rm BB} = 0.18 \pm 0.03$ keV. Although a purely nonthermal model could not be formally excluded, the resulting power-law photon index was unusually soft, $\Gamma = 5^{+5}_{-1}$, indicating a likely thermal spectrum (Spiewak et al. 2016).

2.3. PSR J0751+1807

PSR J0751+1807, an MSP with $P = 3.48$ ms, was discovered by the Arecibo Observatory in a search targeting unidentified Energetic Gamma Ray Experiment Telescope (EGRET) sources (Lundgren et al. 1995). The MSP is in a 6 hr binary system with a helium white-dwarf companion. Initial mass measurements via radio timing detection of orbital decay and Shapiro delay resulted in an NS mass of $2.1 \pm 0.2\, M_\odot$ (Nice et al. 2005). However, more recent radio timing observations found a significantly different NS mass of $1.64 \pm 0.15\, M_\odot$ and a companion mass of $0.16 \pm 0.01\, M_\odot$ (Desvignes et al. 2016). The reported parallax distance of this MSP is $D = 1.07^{+0.24}_{-0.17}$ kpc. Finally, its spin down $\dot{P} \approx 0.8 \times 10^{-20}$ s s^{-1} implies a surface dipole magnetic field strength of $B \approx 1.7 \times 10^8$ G. In the X-ray waveband, the *XMM* spectrum is well described by a power law with photon index $\Gamma = 1.6 \pm 0.2$ (Webb et al. 2004b), but not by a single blackbody, which suggests the possibility of a nonthermally emitting MSP. These data also showed a hint of pulsations at the 1.7σ confidence level.

2.4. PSR J1012+5307

PSR J1012+5307 was discovered with the Lovell radio telescope at Jodrell Bank Observatory (Nicastro et al. 1995). This 5.26 ms pulsar is in an orbit with a low-mass helium white dwarf (van Kerkwijk et al. 1996). While some orbital parameters (e.g., $P_{\rm orb} \approx 0.6$ day) were measured in the discovery observation, they have since been refined (Fonseca et al. 2016). Using the radial velocity curve of the companion, as well as the companion mass (determined via optical spectroscopy), Callanan et al. (1998) estimated the pulsar mass to be $1.64 \pm 0.22\, M_\odot$, and a more recent estimate resulted in $1.83 \pm 0.11\, M_\odot$ (Antoniadis et al. 2016). Having an independent mass measurement makes this pulsar a potentially interesting *NICER* target for radius measurements. The X-ray spectrum of PSR J1012+5307, obtained with *XMM-Newton*, is consistent with both absorbed power law ($\Gamma \sim 1.8$) and absorbed blackbody models (Webb et al. 2004b). If the emission is thermal, the blackbody temperature, $kT_{\rm BB} = 0.26 \pm 0.04$ keV, is consistent with that of other similar MSPs.

Webb et al. (2004b) also reported a 3σ detection of X-ray pulsations at the spin frequency of the pulsar. The distance to this pulsar has recently been updated by identifying the optical counterpart in the *GAIA*-data release 2 (DR2) catalog, resulting in a distance measurement of 907 ± 131 pc when combining the *GAIA* parallax with various other measurements (Mingarelli et al. 2018).

2.5. PSR J1552+5437

PSR J1552+5437 was recently discovered in the radio band with the Low-Frequency Array (LOFAR; van Haarlem et al. 2013) in an unassociated *Fermi*-LAT γ-ray source. This $P = 2.43$ ms pulsar was the first MSP to be discovered at low radio frequencies (115–150 MHz, Pleunis et al. 2017), and its timing solution was used to confirm the presence of pulsations at the same spin period in the original *Fermi* LAT source 3FGL J1553.1+5437. No X-ray counterpart was detected in a short 2.9 ks observation with the *Neil Gehrels Swift Observatory*. No optical counterpart is known for this pulsar.

2.6. PSR J1744−1134

Discovered in the Parkes 436 MHz survey of the southern sky (Manchester et al. 1996), this nearby $P = 4.08$ ms pulsar is now routinely observed for pulsar timing array purposes (e.g., Reardon et al. 2016; Arzoumanian et al. 2018). The X-ray counterpart of PSR J1744−1134 was discovered in *ROSAT* data (Becker & Trümper 1999). It has since been observed by *Chandra*, with the X-ray spectrum likely indicating thermal emission with blackbody temperature of $kT_{BB} \sim 0.3$ keV (Marelli et al. 2011). No optical counterpart has been found despite deep searches, setting an upper limit of $V < 26.3$ (Sutaria et al. 2003).

2.7. PSR J2241−5236

PSR J2241−5236 is another pulsar discovered among *Fermi* LAT unidentified γ-ray sources (Keith et al. 2011). It has a spin period of 2.19 ms. It is classified as a black-widow pulsar with intra-binary shock, in a 3.5 hr orbit with a $M > 0.012 M_\odot$ companion, at a dispersion measure distance of 0.960 kpc (Yao et al. 2017). A *Chandra* observation of PSR J2241−5236 identified a soft X-ray source with a spectrum described by two blackbodies with temperatures of $kT_{BB} \sim 0.07$ keV and ~ 0.26 keV (Keith et al. 2011).

2.8. Other Thermally Emitting MSPs

The following other MSPs were also observed with *NICER*, but their results are not reported in this Letter.

1. PSR J1231−1411, a 3.68 ms pulsar, was discovered in a search campaign of unassociated *Fermi*-LAT sources with the GBT (Ransom et al. 2011). With a 0.2–12 keV flux of 1.9×10^{-13} erg cm^{-2} s^{-1}, it is the third-brightest thermally emitting MSP and thus a target well suited for NS compactness measurement with *NICER*. The pulsar is in a 1.86 days orbit with a low-mass white dwarf (Ransom et al. 2011), possibly associated with a magnitude $g = 25.4$ optical counterpart (Testa et al. 2015). X-ray pulsations from PSR J1231−1411 were detected, but are reported in detail elsewhere (Bogdanov et al. 2019; Ray et al. 2019b).
2. PSR J1614−2230 was discovered in a Parkes radio search targeting unidentified EGRET sources (Hessels et al. 2005;

Crawford et al. 2006). It is an MSP with $P = 3.15$ ms bound to a massive white-dwarf companion in a $P_b = 8.7$ days orbit. The pulsar is particularly important for the *NICER* mission because it is one of the most massive NSs known (Miller 2016), with $M = 1.908 \pm 0.016 M_\odot$ (Arzoumanian et al. 2018). X-ray pulsations from this pulsar were detected with *NICER*, but are reported in full detail elsewhere (Z. Arzoumanian et al. 2019, in preparation), confirming a $\sim 4\sigma$ detection in *XMM* data (Pancrazi et al. 2012).

3. PSR J0740+6620 is another GBNCC-discovered pulsar, in a 4.77 days orbit with a white-dwarf companion (Stovall et al. 2014; Lynch et al. 2018; Beronya et al. 2019). An intense timing campaign with the GBT permitted detection of a Shapiro-delay signal, resulting in a pulsar mass $2.14^{+0.10}_{-0.09} M_\odot$ (Cromartie et al. 2019). Although with somewhat large uncertainties, the high NS mass puts this pulsar on a par with PSR J1614−2230 for dense matter EOS constraints (Miller et al. 2019). The *NICER* observations of this pulsar are also reported in Z. Arzoumanian et al. (2019, in preparation).

3. Observations and Data Reduction

3.1. NICER X-Ray Timing Instrument, Data Filtering, and Pulse Phase Assignments

We observed the seven MSPs listed in Section 2 using *NICER*. Table 2 presents these data, giving the ObsIDs used, the total exposure accumulated, and the total exposure available after filtering. We processed all the data available until 2019 March 23 with `HEASOFT` v6.23 and the *NICER* specific package `NICER-DAS` v3. We filtered the raw data with the standard criteria:

1. pointing offset is $<0°.015$ from the source,
2. pointing $>20°$ from the Earth limb ($>30°$ in the case of a bright Earth),
3. excluding South Atlantic Anomaly passages,
4. selecting events in the 0.25–12 keV energy range.

Additional filtering was necessary to ensure minimal contamination from non-astrophysical background. First, we excluded detectors with `DET_ID` 14, 34, and 54—these are known to be more sensitive to optical loading than others, complicating analyses for soft sources such as our MSPs. Then, we used a filtering criterion based on the rate of "overshoots" (representing large deposition of energy within a detector, and defined by the housekeeping parameter `FPM_OVERONLY_-COUNT`) and on the magnetic cutoff rigidity (`COR_SAX`, in GeV/c). An empirical relation was found to minimize periods of high background, even at low cutoff rigidities, in order to maximize the exposure. For each pulsar, we excluded observed time intervals with the conditions[20]:

$$\mathtt{FPM\_OVERONLY\_COUNT} > (1.52 \times \mathtt{COR\_SAX}^{-0.633})$$
$$\text{and } \mathtt{FPM\_OVERONLY\_COUNT} > 1.0.$$

Some pulsars required slightly different filtering options. For example, a portion of the exposure for PSR J1552+5437 was acquired with a pointing offset $>0°.015$, and therefore this condition was relaxed to include pointing offset $<0°.1$. When

---

[20] The filtering criteria on `FPM_OVERONLY_COUNT` are adopted into the standard `NICERDAS` pipeline as of version 6.0 (https://heasarc.gsfc.nasa.gov/docs/nicer/nicer_analysis.html).

Table 2
NICER Observations of Selected Millisecond Pulsars

Targeted Pulsar	ObsID Range	Raw Exp. (ks)	Std. Filt. Total Exp. (ks)	Opt. Filt. Total Exp. (ks)
PSR J0614−3329	0030050101–0030050110	82	188	181
	1030050101–1030050158	151		
	2030050101–2030050103	29		
PSR J0636+5129	1030070101–1030070197	403	399	347
	2030070101–2030070107	40		
PSR J0751+1807	1060030101–1060030217	462	443	424
	2060030201—2060030211	51		
PSR J1012+5307	0070040101–0070040113	45	590	548
	1070040101–1070040215	570		
	2070040201–2070040212	54		
PSR J1552+5437	1033180102–1033180116	75	72	⋯
PSR J1744−1134	0030160101–0030160109	16	71	⋯
	1030160101–1030160125	62		
	2030160101–2030160106	5		
PSR J2241−5236	1031010101–1031010182	254	113	100
	2031010101	3		

Note. These ObsIDs include all observations acquired from the beginning of the mission (2017 July) through 2019 March 23. The exposure time columns report, from left to right, the total duration of data collection ("Raw"), the exposure time after the standard filtering described in Section 3 ("Std. Filt."), and the final exposure time resulting from the GTI sorting optimization ("Opt. Filt."). For J1552+5437 and J1744−1134, no optimized exposure time is given because no detection is claimed (see Section 4).

necessary, these additional criteria are described for each pulsar in Section 4.

Finally, the pulse phase of each photon was computed using the pulsar timing analysis software PINT (task `photonphase`), given the ephemeris for the pulsar of interest (see Appendix B). Note that `photonphase` computes the transformation from the Terrestrial Time (TT) standard used for time tagging of *NICER* events to Barycentric Dynamical Time (TDB) using the *NICER* orbit files (provided as one of the standard products for each ObsID) and the pulsar astrometric parameters (position, proper motion, and parallax) provided in the epheremides—only the solar system ephemeris has to be specified (DE421 or DE436). The H-test is then employed to quantify the presence of pulsations (de Jager et al. 1989; de Jager & Büsching 2010), either in the full band or in the soft X-ray band (0.25–2.0 keV), setting a 3σ single-trial limit to claim the detection of pulsations. We report the detections and non-detections of pulsations in Section 4. Despite our stringent filtering described above, the background, variable throughout the ObsIDs, may still contaminate significantly the pulse profiles of the detected pulsars. We describe in the next section a method of good time interval (GTI) selection to minimize background contamination and provide cleaner pulse profiles.

3.2. GTI Sorting Method

Because each *NICER* exposure occurs under different observing conditions (pointing with respect to the Sun, Earth, or Moon, location of the ISS, space weather, etc.), the amount of non-astrophysical background can vary greatly between ObsIDs, and even within single ObsIDs. Faint sources, such as the MSPs studied in this Letter, are most affected by background: GTIs with low background improve the S/N, while those with high background dilute the pulsations and decrease the S/N. To minimize the background contamination and maximize the S/N, we therefore only consider the GTIs
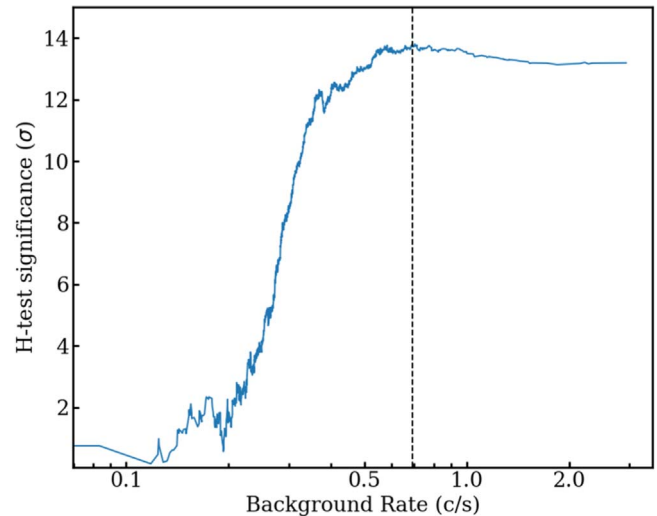

Figure 1. Evolution of the pulsation detection significance (units of σ) as a function of the GTIs sorted by total count rate, equivalent to the cumulative exposure time (totaling 181 ks), for PSR J0614−3329. The dashed vertical line indicates the optimal GTI cut that maximizes the detection significance. In other words, adding GTIs to the left of this line increases the detection of pulsations, while adding high-background GTIs, to the right of the line, decreases the detection significance.

with low background. This is done by splitting the GTIs into small segments of at least 10 s (to have a good estimate on the background count rate) and at most 100 s. These GTIs are then ordered by their corresponding total count rate, which we use as a proxy for the background rate as the MSP contribution to the total rate is of the order of a few percent and is constant. We employ the H-test to quantify the significance of the pulsations. We do so cumulatively on the sorted GTIs (from the lowest to the highest count rate). This is illustrated in Figure 1 for

Table 3
Results of the Pulsation Searches

Pulsar	Single-trial H-test Significance[a]	GTI opt. H-test Significance[b]	Energy Range (keV)	Pulsed count rate[c] (s^{-1})
PSR J0614−3329	11.0σ	14.0σ	0.33–1.43	0.027 ± 0.002
PSR J0636+5129	4.3σ	5.5σ	0.27–0.91	0.008 ± 0.001
PSR J0751+1807	6.5σ	8.5σ	0.32–1.82	0.014 ± 0.001
PSR J1012+5307	3.0σ	4.7σ	0.31–1.94	0.007 ± 0.001
PSR J1552+5437	1.5σ	*No detection*	...	...
PSR J1744−1134	2.5σ	*No detection*	...	...
PSR J2241−5236	6.3σ	7.4σ	0.41–1.14	0.020 ± 0.002

Notes. The results for PSR J1231−1411, PSR J0740+6620, and PSR J1614−2230 are reported elsewhere (Ray et al. 2019b and Z. Arzoumanian et al. 2019, in preparation).
[a] Single-trial H-test significance in the 0.25–2.0 keV energy range.
[b] H-test significance after optimization of the GTI and energy band (see Section 5 for a short discussion of the number of trials).
[c] Pulsed count rates are provided in the optimal energy range provided for each pulsar.

PSR J0614−3329, which shows the cumulative H-test significance as a function of GTIs with increasing background count rates. The H-test significance first increases as low-background GTIs are added and then stabilizes or decreases when higher-background GTIs are being included. This methods permits finding the optimal cut (indicated by the vertical line in Figure 1) that maximizes the H-test significance by excluding GTIs with the highest background rates.

To further increase the pulse profiles S/N, i.e., reducing the background contributions, additional improvement can be achieved by optimizing the selected energy range. In some GTIs, optical loading may cause a sharp increase of the count rate below ∼0.4 keV. Excluding part or all of the 0.25–0.4 keV energy range may therefore further increase the detection significance of the pulsations. Similarly, because the thermal spectra of MSPs are expected to drop rapidly above ∼1.5 or 2 keV, an optimization of the high-energy cutoff can minimize the background contribution to the pulse profiles. Here, we perform a grid search for the low- and high-energy cutoffs (with ranges 0.25–1.0 keV and 0.9–3.0 keV, respectively) and the resulting optimal energy ranges are reported in Table 3.

3.3. Nançay Radio Telescope (NRT) Pulsar Timing Data

Timing solutions for all pulsars, except PSR J1552+5437 and PSR J2241−5236, have been constructed by analyzing pulsar observations made with the Nançay Ultimate Pulsar Processing Instrument (NUPPI) in operation at the *NRT* since 2011 August. In these observations, 512 MHz of frequency bandwidth are recorded in the form of 128 channels of 4 MHz each, which are coherently de-dispersed in real time and phase-folded at the expected topocentric periods of the observed pulsars (see Guillemot et al. 2016, for additional details on pulsar timing observations with the NUPPI backend). We considered timing observations made at 1.4 GHz, which represent the bulk of pulsar observations with *NRT*. For each pulsar, we used all of the available NUPPI data through 2019 June.

Data reduction steps were performed using the PSRCHIVE software library (Hotan et al. 2004). We cleaned the data of radio frequency interference and calibrated the observations in polarization using the SINGLEAXIS method. High-S/N profiles were built by summing up the 10 best detections of each pulsar, and times of arrival (TOAs) were extracted by cross-correlating

the observations with smoothed versions of the summed profiles. For each NUPPI observation, we formed one TOA per 128 MHz of bandwidth. The TOAs at multiple frequencies enabled us to track potential variations of the dispersion measure (DM). We used the TOA data sets and the TEMPO2 pulsar timing package (Hobbs et al. 2006) to build timing solutions for each pulsar, fitting for their astrometric, rotational, and DM parameters, as well as orbital parameters for those pulsars in binary systems. The timing solutions, presented in Appendix B, obtained with this procedure describe the TOAs appropriately. We note that these timing solutions are sufficient for the purpose of calculating the phases of X-ray photons, as done in this Letter, over the span of NICER's data collection, but they might not be the most optimal solution for long-term timing of these pulsars.

3.4. Parkes Pulsar Timing Data

Timing solutions for PSR J2241−5236 made use of data collected with the Parkes Radio Telescope, primarily for the Parkes Pulsar Timing Array (project P456). The observing strategy is described in Reardon et al. (2016), and the data reduction by Kerr et al. (2018), but we summarize them here. Observations of 64 minutes duration are performed with approximately a three-week cadence in three radio frequency bands, typically centered on 732, 1369, and 3100 MHz. Down-converted voltages are digitized, converted to spectra via a polyphase filterbank, and autocorrelated to form Stokes parameters. These multi-channel time series are folded at the known pulsar spin periods into pulse profiles and integrated for 64 s before output for archiving. Observations of a pulsed noise diode enable gain and polarization calibration. Data are reduced using PSRCHIVE and TOAs extracted using an analytic profile. As described above, timing solutions are prepared with TEMPO2. To enable absolute alignment of the radio and X-ray profiles, we selected a single high S/N TOA to serve as the reference epoch (the TZRMJD parameter; see Section 5.2). The timing solution makes use of radio data collected between 2010 February 9 and 2018 April 22, requiring extrapolation to fold *NICER* data acquired outside of this epoch. We verified the timing solution on ad hoc data acquired through 2018 November 10 and observed no substantial deviations of these pulse arrival times from the predicted phase.

4. Results

The results of the pulsation searches are presented in Table 3, which contains the single-trial detection significance, the H-test significance after GTI optimization, and the optimal energy range for each observed MSP. The optimization of the energy range permitted finding the low-energy cut, which depends on how much optical loading noise is present, as well as the high-energy cut, which depends primarily on the brightness of the MSP (and its spectral shape, i.e., surface temperature). Five out of the seven pulsars show pulsations in the soft X-ray band, with a single-trial significance (before GTI optimization) $>4.3\sigma$, except for PSR J1012+5307 (at 3σ). With the GTI optimization described above, the H-test significance for the detected pulsars are all $>4.7\sigma$. The two non-detected pulsar have single-trial H-test significance of 1.5σ and 2.5σ for PSR J1552+5437 and PSR J1744−1134, respectively.

4.1. PSR J0614−3329

For this pulsar, a simple phase-folding of the events with a recent ephemeris (Table 5) in the full *NICER* energy range resulted in a significant 7.5σ single-trial detection of the pulsations, and 11σ when selecting events in the soft (0.25–2.0 keV) band. Optimization of the GTIs (see Section 3.2) improved the significance to 11.4σ. A grid search in energy concluded that the 0.33–1.43 keV energy range is optimal, resulting in a 14σ significance, for a total exposure time of 181 ks. The pulse profile is shown in Figure 2, together with the *NRT* pulse profile at 1.4 Ghz from the data used to generate the timing solution.

4.2. PSR J0636+5129

The standard filtering described in Section 3 leaves 400 ks of exposure for PSR J0636+5129. After folding all events in the 0.25–12.0 keV with an ephemeris from *NRT* observations (Table 6), the H-test significance of 2.5σ is not sufficient for a confident claim of detection. However, restricting the energy range to the soft 0.25–2.0 keV band brings the detection significance to 4.3σ, and shows a broad single pulse. Further improvement is obtained with our GTI optimization, which results in 5.5σ H-test significance for a total of 347 ks of good exposure. The pulse profile, obtained in the 0.27–0.91 keV optimal energy range, is shown in Figure 2.

4.3. PSR J0751+1807

Observations of PSR J0751+1807 were performed with an offset pointing, in an effort to minimize contamination from nearby sources. Using archival *XMM* data and sources in the 3XMM-DR8 catalog (Rosen et al. 2016), we determined the exact position to maximize the S/N for the pulsar—see Appendix A for the results of the pointing offset determination, and see Bogdanov et al. (2019) for a description of the method.

In the case of PSR J0751+1807, the initial single-trial H-test significance after standard filtering and folding (see ephemeris in Table 7) is 4.1σ in the full 0.25–12.0 keV range. This detection increases when using only events in the 0.25–2.0 keV soft band, where thermal emission would be the strongest. There, we obtain a detection significance of 6.5σ. Finally, as done above for the other pulsars, the GTI optimization further improves the H-test significance: 7.5σ (0.25–2.0 keV), and

8.5σ when the optimal energy range of 0.32–1.82 keV is used. The pulse profile, resulting from 424 ks of selected GTIs is shown in Figure 2. Our confident detection confirms the marginal 1.7σ detection claimed from early *XMM* data of this pulsar (Webb et al. 2004b).

4.4. PSR J1012+5307

A 590 ks exposure of PSR J1012+5307 was obtained with *NICER*, after standard filtering. However, after event folding with the ephemeris of Table 8, the X-ray pulsations remain undetected in the full 0.25–12 keV band ($\sim2\sigma$), and marginally detected (3σ) when using soft-band photons only. A fraction of the exposure, early in the mission, was obtained at low Sun angles, close to the instrument's 45° limit. Our GTI optimization helps to minimize the impact of exposures with high optical loading background, such as those at low Sun angles. Applying this optimization improves the H-test significance to 3.7σ in the 0.25–2.0 keV band, and 4.67σ when also optimizing the energy range—we find that 0.31–1.94 keV is optimal. A total of 548 ks of exposure, out of the 590 ks available, is selected to generate the optimal pulse profile for PSR J1012+5307 (Figure 2). Although the detection of the pulsations in the *NICER* data is somewhat marginal, our observations confirm the 3σ detection in *XMM-Newton* data (Webb et al. 2004b). While the apparent X-ray/radio peak separation, ~0.3 phase, is consistent between the *XMM* and *NICER* data sets, the double peak structure of the *XMM* data (Figure 9 of Webb et al. 2004b) is not evident in the *NICER* data.

4.5. PSR J1552+5437

NICER observed this pulsar for a total of 72 ks after standard filtering. Unfortunately, a record-keeping error resulted in the use of incorrect pointing coordinates, offset $\sim2'.4$ from the pulsar's reported position (Pleunis et al. 2017). Therefore, the standard angular distance filtering criterion (excluding $>0'.9$) had to be relaxed during the processing; the other standard filtering criteria (Section 3) were retained, resulting in 69 ks of good exposure, but with reduced sensitivity to the off-axis source. After folding with the ephemeris of Table 9, the single-trial detection significance is $\sim1.5\sigma$ whether we choose the full energy range or the soft band only. Applying the GTI optimization increases the significance to 3σ and 2.8σ for these two cases, respectively; however, only small fractions of the total exposure (6 ks and 28 ks, respectively) are retained by the optimization. Optimizing both sorted GTIs and the energy range also leads to an unrealistically small selection of GTIs (resulting in only 140 events out of $\sim67,000$).

Overall, we conclude that no pulsations were firmly detected from this pulsar. Assuming that the detection is real, however, the pulsations would correspond to a pulsed count rate of 0.008 ± 0.004 c s^{-1} (consistent with a non-detection of pulsations), which is equivalent to a *Swift*-X-Ray Telescope (XRT) rate of 0.0004 c s^{-1}. One would therefore expect 1.2 counts in a 2.9 ks *Swift*-XRT exposure, which is consistent with the *Swift* non-detection. Longer *NICER* observations, with the correct pointing, are warranted to confirm or refute the possible presence of X-ray pulsations from this pulsar, or alternatively, longer X-ray imaging observations are required to determine the actual existence of X-ray emission from this pulsar.[21]

---

[21] *NICER*-XTI is a non-imaging instrument, and the detection of a faint pulsar can be confirmed with certainty from the detection of its pulsations.
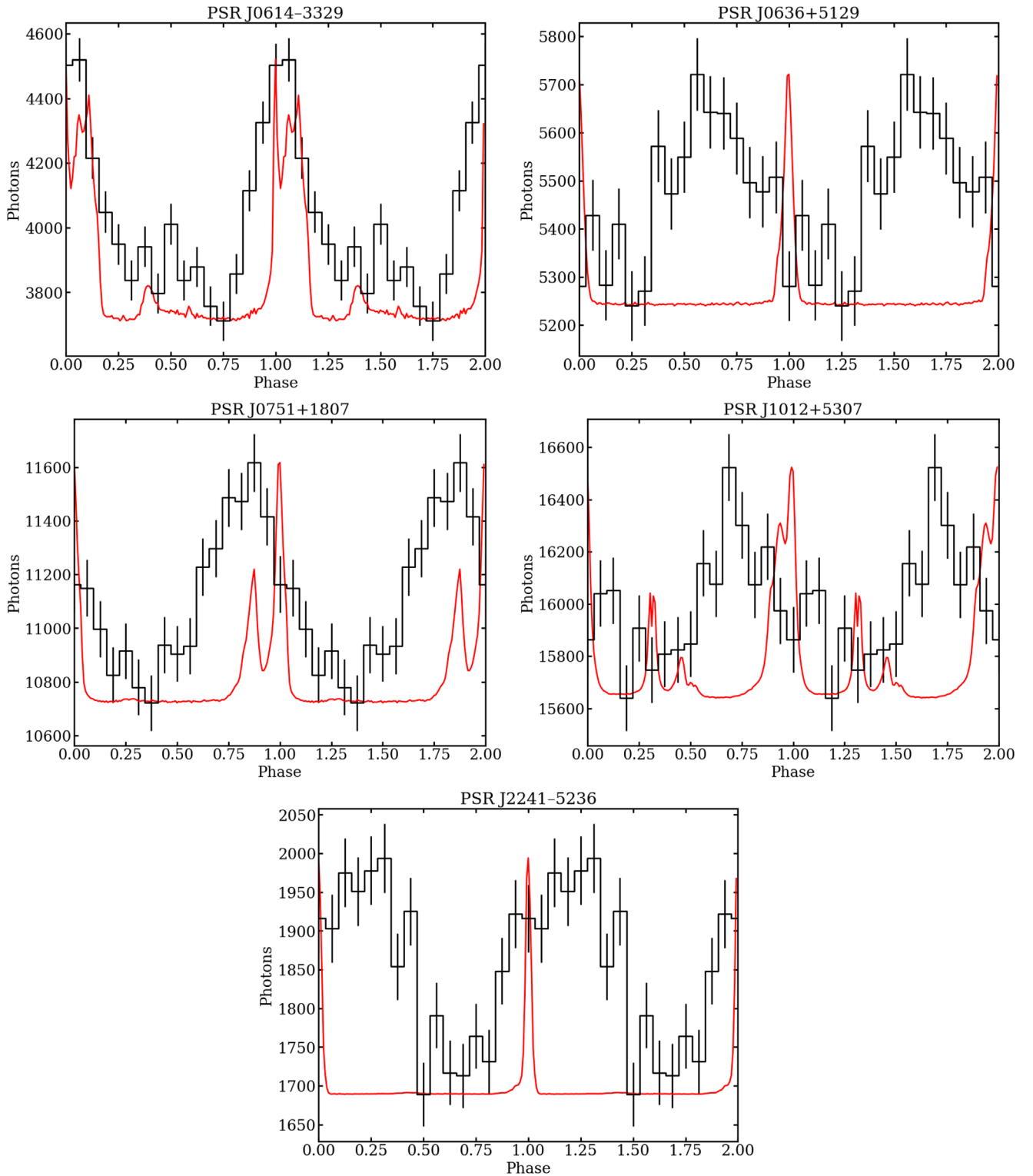
Figure 2. *NICER* pulse profiles (black, 16 bins per phase) for the five pulsars with detected pulsations (obtained in their respective optimal energy ranges, see Table 3), together with their radio pulse profile at 1.4 GHz (red) from the *Nançay* or *Parkes* radio telescopes. The ephemerides used for folding are presented in Tables 5 through 11, respectively. Two rotational cycles are shown for clarity.

4.6. PSR J1744−1134

A total of 71 ks of exposure are available for this pulsar after standard filtering. The ephemeris from the *NRT* (Table 10) allows us to calculate the pulse phase of each photon. However, whether we choose the full energy band or the 0.25–2.0 keV range, or we attempt to optimize it, the detection significances remain 2.3σ, 2.5σ, and 2.7σ, respectively. Optimization of the GTIs to exclude those with high background also results in low-significance detections of pulsations and unrealistically small selections of GTIs (<few ks). We therefore conclude that no pulsations are seen from PSR J1744−1134. Past observations of this pulsar, obtained with *Chandra*, do not have the

Table 4
Pulsed Thermal Luminosities, Spin-down Luminosities, and Efficiencies

Pulsar	$n_{\rm H}$ $(10^{20}\ {\rm cm}^{-2})$	$kT_{\rm BB}$[a] (keV)	$F^{\rm pulsed}_{0.2-10.0\,{\rm keV}}$ (erg cm^{-2} s^{-1})	$L^{\rm pulsed}_{0.2-10.0\,{\rm keV}}$ (erg s^{-1})	$\dot{E}$ (erg s^{-1})	$L_X/\dot{E}$ (10^{-4})
PSR J0614−3329	3.0	0.23	3.5×10^{-14}	3.0×10^{31}	2.4×10^{34}	13.0
PSR J0636+5129	9.5	0.18	2.1×10^{-14}	1.0×10^{29}	5.6×10^{33}	0.2
PSR J0751+1807	6.2	0.10	3.2×10^{-14}	4.4×10^{30}	5.7×10^{33}	7.7
PSR J1012+5307	0.8	0.26	7.8×10^{-15}	7.7×10^{29}	2.7×10^{33}	2.9
PSR J2241−5236	1.1	0.26	3.2×10^{-14}	3.5×10^{30}	2.5×10^{34}	1.4

Notes. The pulsed X-ray fluxes and luminosities reported are unabsorbed. The luminosities are calculated with the distances reported in Table 1. The $\dot{E}$ values reported have been corrected for the Shklovskii effect (Shklovskii 1970).
[a] We assumed a 0.1 keV blackbody for PSR J0751+1807, and the values presented in Section 2 for the others.

timing resolution necessary to confirm or refute our conclusions.

4.7. PSR J2241−5236

The phase-folding of event times from PSR J2241−5236 leads to pulsations detected with a single-trial significance of 4.5σ when considering the full *NICER* band, and 4.9σ when using 0.25–2.0 keV photons. GTI optimization permits excluding periods of high background and increases the significance to 6.3σ (0.25–2.0 keV). Finally, the grid search described above to find the optimal energy range yields 0.41–1.14 keV, i.e., excluding the range where the optical loading is the strongest, and resulting in pulsations with a significance at the 7.4σ confidence level. Using these 100 ks of optimally selected GTIs, we provide the pulse profile for PSR J2241−5236, along with the Parkes Radio Telescope pulse profile, in Figure 2.

4.8. PSR J0740+6620, PSR J1231−1411, and PSR J1614−2230

The detection of X-ray pulsations from J1231−1411 has been reported in Ray et al. (2019b) and Bogdanov et al. (2019), while PSR J1614−2230 is the subject of another article in preparation (Z. Arzoumanian et al. 2019, in preparation), confirming the detection reported in Pancrazi et al. (2012). The *NICER* observations of PSR J0740+6620 are also presented in Z. Arzoumanian et al. (2019, in preparation).

5. Discussion and Conclusion

5.1. Thermal Luminosity versus Spin-down Luminosity

From the pulsed count rates listed in Table 3, deduced from the pulse profile after GTI and energy range optimizations, we estimated with WebPIMMS[22] the pulsed X-ray unabsorbed flux and luminosity (with distances from Table 1) for the MSPs with detected pulsations. To do so, we used the blackbody temperatures published in the literature (see Section 2, or assuming $kT_{\rm BB} = 0.1$ keV for PSR J0751+1807). We also assumed the value of hydrogen column density $n_{\rm H}$ obtained from neutral H maps using the HEASARC $n_{\rm H}$ tool[23] (with the most recent maps from HI4PI Collaboration et al. 2016). These pulsed luminosities are listed in Table 4 together with spin-

down luminosity $\dot{E}$ (corrected for the Shklovskii effect). We find efficiencies $L_X/\dot{E}$ in the range 10^{-5}–10^{-3}, which are similar to those of other MSPs (e.g., Figures 9 and 10 in Lee et al. 2018), but the values that we report in Table 4 should be viewed as lower limits as they were derived from the pulsed flux only.

5.2. Radio/X-Ray Phase Separation

Producing properly phase-aligned radio and X-ray pulse profiles can be challenging. For most radio pulsar timing studies an overall absolute phase error is irrelevant, but for alignment with other wavebands, correct absolute timing is critical, so we provide some detail here. In this work, the phase 0.0 is defined by the radio template used to extract the radio TOAs. The *NRT* templates are aligned such that the peak of the main pulse is the fiducial point. Pulsar timing codes (`TEMPO`, `TEMPO2`, and `PINT`) produce a fictitious TOA that has zero residual to the model (with its time, observing site, and frequency defined by the `TZRMJD`, `TZRSITE`, and `TZRFRQ` parameters). The PINT `photonphase` task or the `TEMPO2` `photons` plugin will assign pulse phases to the X-ray photons using this reference. Possible sources of error include: (1) uncertainty in extrapolating from the radio arrival time to infinite frequency because of dispersion measure uncertainty; (2) uncalibrated cable or pipeline delays in data taking systems; (3) inconsistent application of observatory clock corrections (e.g., confusion over whether `TZRMJD` is in observatory clock time or UTC); (4) using different ephemerides or positions when barycentering the two data sets, etc.

The phase alignments shown in Figure 2 are made with the timing models presented in this Letter (Tables 5–11). To provide a cross check for potential errors in the alignment procedure, we reproduced Figure 2 for PSR J0636+5129 and PSR J1012+5307 using timing models from NANOGrav (Arzoumanian et al. 2018), which are from the GBT, instead of *NRT*. We obtained very similar profiles and peak separations, giving us confidence that the alignments presented in Figure 2 are correct; in particular, that the clock corrections from *NRT* are properly taken into account by the PINT `photonphase` task.

We use the Fourier decompositions presented in Figure 3 to determine the phase of the X-ray pulses and therefore the phase offset $\Delta\phi$ with the radio peak.

   1. PSR J0614−3329: Both X-ray and radio main peak are broad and essentially aligned ($\Delta\phi \sim 0.07$).

---

[22] Available at https://heasarc.gsfc.nasa.gov/cgi-bin/Tools/w3pimms/w3pimms.pl.
[23] Available at https://heasarc.gsfc.nasa.gov/cgi-bin/Tools/w3nh/w3nh.pl. Although these values are integrated along the line of sight through the Galaxy, all five pulsars are >18° above the Galactic plane and these $n_{\rm H}$ values should be reasonable estimates.
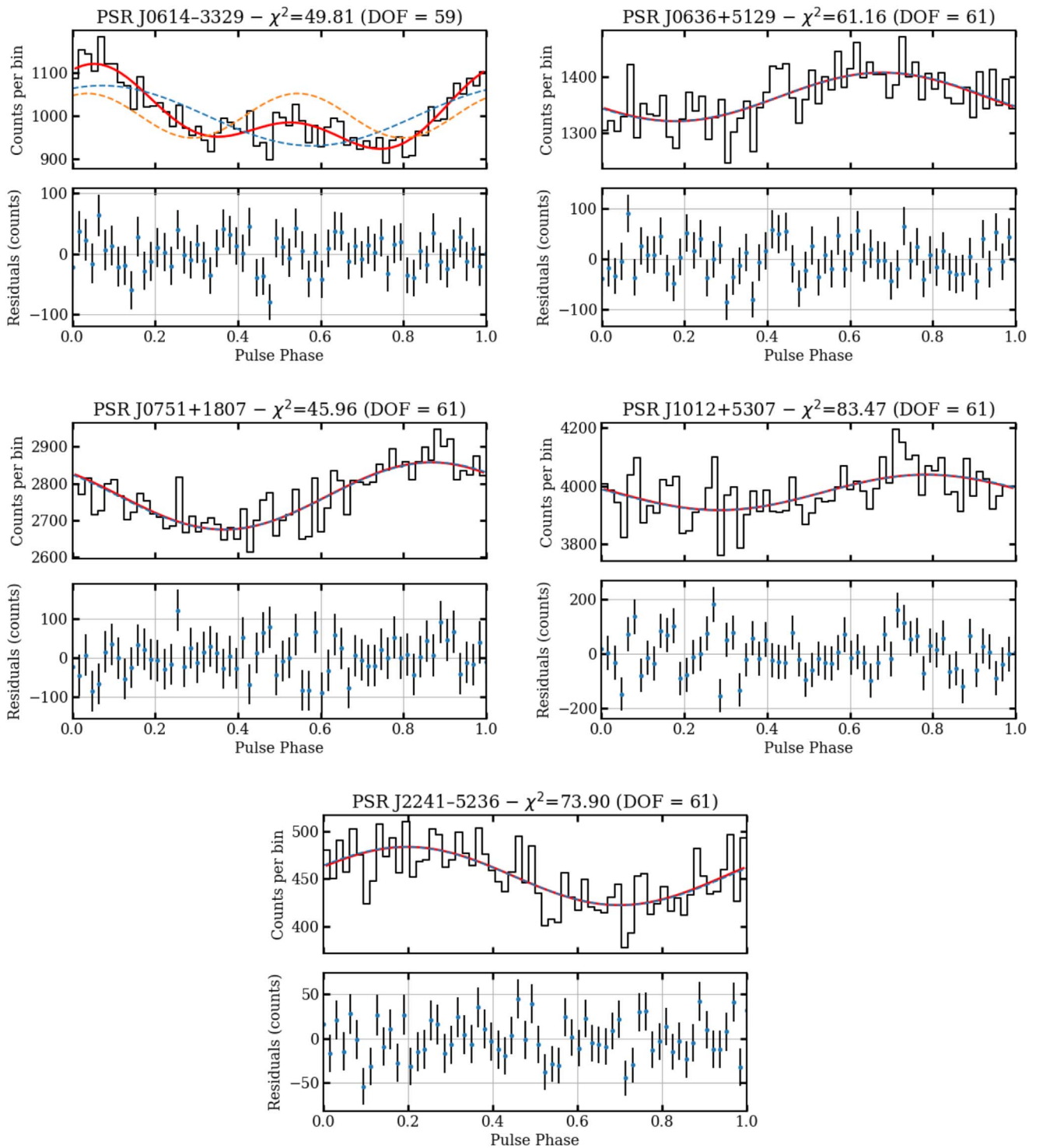
Figure 3. Fourier decomposition of the *NICER* pulse profiles of the five MSPs with detected pulsations, with 64 phase bins. Only PSR J0614−3329 required more than one harmonic. In each panel, the dashed lines are the harmonic components, and the red solid line is the sum of the components. The bottom plot of each panel shows the residuals. Only one rotational cycle is shown.

Furthermore, the secondary radio peaks appear to be somewhat aligned with the secondary X-ray pulse (see Figure 2).

2. PSR J0636+5129: The seemingly broad and asymmetric X-ray profile (fast rise and slower decay) of this pulsar leads the radio pulse by $\Delta\phi \sim 0.3$–0.4.

3. PSR J0751+1807: The main radio pulse lags the X-ray peak by $\Delta\phi \sim 0.1$. However, a "precursor" radio pulse

precedes the main radio pulse by ~ 0.1 in phase, and is therefore aligned with the X-ray pulse.

4. PSR J1012+5307: This pulsar also displays a large offset, with the X-ray pulse leading the main radio pulse by $\Delta\phi \sim 0.3$, while the secondary radio pulses fall in the trough of the X-ray profile.

5. PSR J2241−5236: The X-ray pulse is broad, with a duty cycle of more than 60%, and a peak that lags the narrow

radio pulse (duty cycle of a few percent at most) by $\Delta\phi \sim 0.2$.

The $\Delta\phi$ offsets in the range 0.2–0.3 for three out of the five MSPs in our sample are in contrast with other MSPs studied with *NICER*. As listed in Section 1, three of the four pulsars presented in Bogdanov et al. (2019) all have near perfect alignment between the X-ray and radio pulses (PSR J0437−4715, PSR J0030+0451, and PSR J1231−1411), while others have misaligned X-ray and radio pulses, such as PSR J1614−2230. The large $\Delta\phi \sim 0.2$–0.3 phase offsets between the radio and X-ray measured in this work may put into question the surface heating patterns and the centered dipolar nature of these MSP magnetic fields. For example, the location of the hot regions, separated by $\sim 65°$ (Riley et al. 2019), at the surface of PSR J0030+0451 suggest a magnetic field that significantly deviates from a simple centered dipolar field (Bilous et al. 2019), even though the X-ray and radio pulses are aligned. Additionally, the observed radio profiles could find their origin in the outer edge (i.e., non-axial) parts of the beam, instead of the core of the beam emission (Lyne & Manchester 1988; Kramer et al. 1999), therefore resulting in an offset with the X-ray pulses coming from the footprints of the magnetic field at the NS surface. Overall, the relationship between the X-ray and radio pulsations of thermally emitting MSPs therefore ought to be studied in more detail, and a more systematic study of radio and X-ray profiles could help constrain the complexity of the magnetic fields in these sources. The phase alignment of the radio and X-ray pulses with the γ-ray pulsations may also be informative, although the latter originates from emission further out in the magnetosphere and does not necessarily align with the radio or X-ray profiles.

5.3. Harmonics in the Pulse Profiles

For the five pulsars with detected pulsations, we apply a Fourier decomposition technique to search for the presence of harmonics in the broad, sine-like profiles. We find that PSR J0614−3329 is the only one that requires two harmonics (using a single harmonic leaves structured residuals and gives $\chi^2_\nu > 2$). For the other four pulsars, a single sine function is sufficient to describe the pulse profile (i.e., $\chi^2_\nu \approx 1$ and white residuals). Figure 3 shows the harmonic fits and residuals for the five pulsars.

The detection of higher harmonics may provide evidence for the various effects that distort the pulses from a simple sinusoid (see below) and/or for the presence of a second visible polar cap (i.e., a secondary pulse, as clearly seen in the case of PSR J0030+0451; Bogdanov & Grindlay 2009). At spin frequencies up to ~ 300 Hz, atmosphere beaming (MSP surface emission is not isotropic), as well as self-occultation of the polar caps by the star, make the pulse profile deviate from a sinusoidal shape. Above 300 Hz, other effects, such as Doppler boosting and aberration, add more power to the harmonic content (Miller & Lamb 2015).

The two harmonics in PSR J0614−3329 can be readily interpreted as due to the presence of a secondary pulse, about half a phase from the dominant pulse (see Figures 2 and 3). This likely originates from a second polar cap, similar to that observed in PSR J1231−1411 and PSR J0030+0451 (Bogdanov et al. 2019). For the other four pulsars of the present study, the single harmonic detected may simply be ascribed to the low S/N of the data sets. For comparison, the key *NICER* targets used for pulse profile modeling (PSR J0437−4715, PSR J0030+0451, PSR J1231−1411, and PSR J2124−3358) show up to four harmonics in their pulse profiles (Bogdanov et al. 2019), thanks to the high S/N provided by deep (~ 1–2 Ms) exposures. Observations with exposures of 1–5 Ms for the five pulsars reported here will likely reveal their full harmonic content and is required to perform pulse profile modeling analyses to extract mass and radius constraints.

5.4. Conclusion and Perspectives

We present a systematic search for X-ray pulsations using *NICER* timing observations of a set of seven nearby rotation-powered MSPs. X-ray pulsations are securely detected from five of the targets. Specifically, the single-trial significance is $>4.3\sigma$ for all MSPs except for PSR J1012+5307 (3σ). This significance is improved ($\geqslant 4.7\sigma$ in all cases) when optimizing the selection of GTIs to favor low background count rates (see Section 3.2). Although the number of trials involved with the GTI sorting method is not straightforward to quantify exactly, it is much less than the number of GTIs for a given MSP data set. Indeed, because they are sorted by increasing total rate, they are highly correlated, making the trial factor for our GTI sorting method on the order of a few.

Because of the low count rates for the MSPs in this Letter (see Table 3), a proper spectral analysis was unfortunately not possible. Using a *NICER* background model (Bogdanov et al. 2019; Ray et al. 2019b), we estimate that $\lesssim 5\%$–10% of the total detected counts in the soft X-ray band (0.5–2.0 keV) originate from the observed pulsars. Given the uncertainties involved with modeling the background,[24] we refrain from providing spectral parameters for these faint pulsars. Imaging instruments sensitive in the soft X-ray band, such as *XMM-Newton*, *eROSITA* (Predehl et al. 2014), or the future *Athena X-ray Observatory* (Nandra et al. 2013), are better suited for such spectral analyses.

The results of this Letter nonetheless enlarge the sample of radio MSPs detected as pulsed X-ray sources—in particular, those with thermal emission. All five MSPs detected have broad pulsed profiles, fitted with one or two harmonics (see Section 5.3). Published studies of these MSPs showed that they also have X-ray spectra consistent with thermal emission[25] (simple or double blackbody; see Section 2 for details). The broad pulses and the spectral shapes lead us to tentatively conclude that we observe thermal X-ray pulsations from these five MSPs. We note that more detailed spectral analyses, with high S/N, is necessary to confirm with certainty the spectral nature of these pulsations. Indeed, PSR J0218+4232 displays a pair of rather broad X-ray pulses (~ 0.25 phase), connected by a "bridge" joining them (Deneva et al. 2019). However, its X-ray spectrum is hard and purely nonthermal (with a power-law photon index $\Gamma \approx 1.1$), making the detection of pulsations possible up to ~ 10 keV in the *NICER* data (Webb et al. 2004a; D. M. Rowan et al. 2019, in preparation). To confirm the thermal nature of the MSPs studied here would require observations with spectro-imaging X-ray instruments.

---

[24] *NICER* is a non-imaging instrument and the background is modeled based on observations of blank-sky exposures, as well as housekeeping and space-weather parameters.

[25] In all five cases, the spectral analyses, reported in the literature, were performed on rather low S/N data from *Swift*-XRT, *XMM*, or *Chandra*, with less than a few hundred of counts.

The detection of pulsations, if they are indeed of thermal origin, seems to confirm that for the majority of MSPs the main source of their X-ray emission comes from their heated polarcaps. The findings of this Letter also make these MSPs promising targets for follow-up X-ray observations with *NICER* and/or with future proposed telescopes such as *STROBE-X* (Ray et al. 2019a) or *eXTP* (Watts et al. 2019), to enable constraints on the NS mass–radius relation and the dense matter EOS via the pulse profile modeling technique. The binary MSPs with independent mass measurements from radio timing, PSR J0751+1807 and PSR J1012+5307, are of particular interest in this sense as they can offer more stringent constraints on the NS radius. PSR J0614−3329, the brightest of the five MSPs studied here, is also a promising target.

Following the discoveries of X-ray pulsations from five MSPs, *NICER* continues to observe these targets to better characterize their X-ray pulse profiles. These MSPs will require a few Ms of exposure per pulsar with *NICER*. Furthermore, *NICER* will also target newly discovered MSPs such as those discovered by the Arecibo PALFA survey (Parent et al. 2019).

Appendix A
Pointing Optimization for PSR J0751+1807

Figure 4 in this Appendix presents the results of the pointing optimization for PSR J0751+1807, as described in Bogdanov et al. (2019).
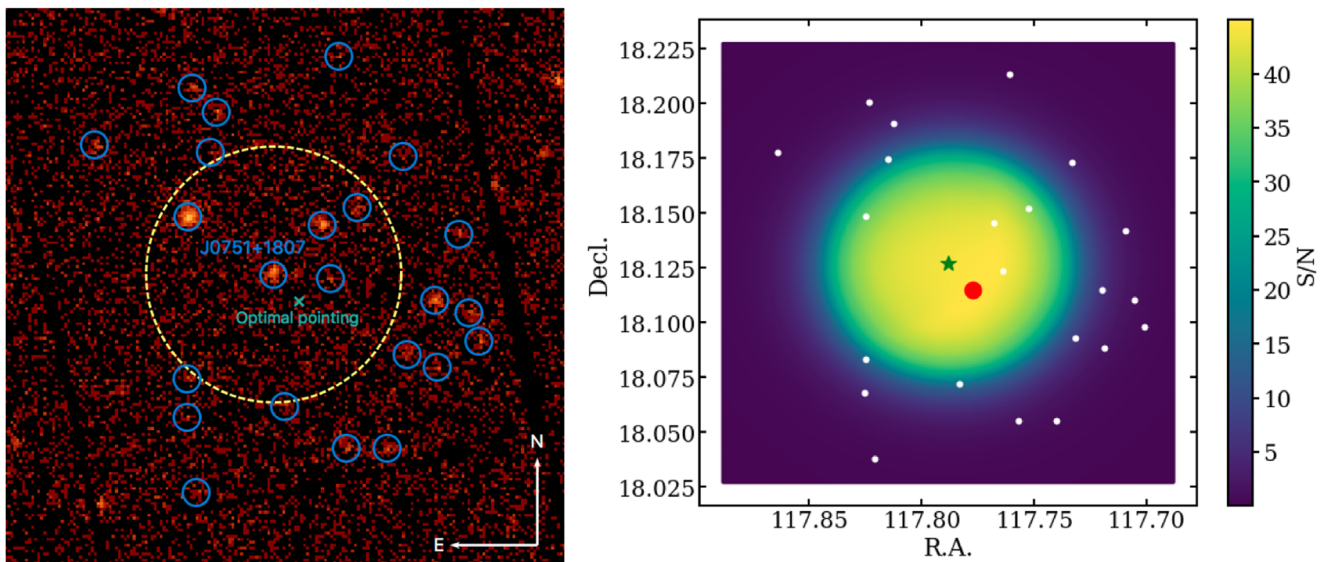

Figure 4. Left panel: *XMM-Newton* EPIC MOS image of PSR J0751+1807 and nearby sources. The teal "×" shows the position of the optimal *NICER* pointing that maximizes the S/N from the pulsar, i.e., minimizes the contamination from all other sources (blue circles) within 6′. The dashed yellow circle shows the size of the *NICER* 6.′2 half-power diameter point-spread function. Right panel: map of the S/N of PSR J0751+1807 as a function of *NICER* pointing. The green star shows the pulsar position, and the red circle shows the calculated optimal pointing position that maximizes the S/N. The optimal pointing is 1′ from the pulsar position and permits a gain in S/N of a few percent.

Appendix B
Millisecond Pulsar Ephemerides

In the following Tables 5–11, we present the ephemerides from the *NRT*, the Parkes Radio Telescope, and *LOFAR* used to calculated the phases of X-ray events detected by *NICER*. We stress that these ephemerides were obtained for the sole purpose of phase-folding X-ray events, and should *not* be used as long-term timing solutions for these pulsars.

Table 5
Ephemeris of PSR J0614−3329 used in this Work and Obtained from Observations with the *NRT*

Parameter	Value
Pulsar name	J0614−3329
R.A. (J2000)	06:14:10.347818(8)
Decl. (J2000)	−33:29:54.1161(1)
Proper motion in R.A. (mas yr^{-1})	0.61(3)
Proper motion in decl. (mas yr^{-1})	−1.74(4)
Epoch of position	56000.0
Spin frequency, ν (Hz)	317.594455162825(3)
Spin frequency derivative, $\dot{\nu}$ (s^{-2})	$-1.75678(1) \times 10^{-15}$
Epoch of period	56000.0
Dispersion measure, DM (pc cm^{-3})	37.050(5)
Dispersion measure derivative, DM1	0.0004(1)
Epoch of DM	56000.0
Binary model	BT[1]
Binary orbital period, P_b (days)	53.584612528(3)
Projected semimajor axis of orbit, x (lt-s)	27.6387906(2)
Orbital eccentricity, e	0.00018080(1)
Epoch of periastron, T0 (MJD)	54986.0699(6)
Longitude of periastron, ω (degrees)	15.938(4)
Terrestrial time standard (CLK)	TT(BIPM2011)
Reference epoch (MJD)	57236.403056165037679
Frequency of reference TOA (MHz)	1299.619019
Solar system ephemeris	DE436

Note. The digit in parenthesis represents the 1σ uncertainty on the last digit.
[1] Blandford & Teukolsky ([1976](#))

Table 6
Ephemeris of PSR J0636+5129 used in this Work and Obtained from Observations with the *NRT*

Parameter	Value
Pulsar name	J0636+5129
R.A. (J2000)	06:36:04.84618(1)
Decl. (J2000)	+51:28:59.9651(3)
Proper motion in R.A. (mas yr^{-1})	3.22(3)
Proper motion in decl. (mas yr^{-1})	−1.61(6)
Epoch of position	56000.0
Spin frequency, ν (Hz)	348.559231746222(3)
Spin frequency derivative, $\dot{\nu}$ (s^{-2})	$-4.1902(2) \times 10^{-16}$
Epoch of period	56000.0
Dispersion measure, DM (pc cm^{-3})	11.0982(1)
Epoch of DM	56000.0
Binary model	ELL1
Binary orbital period, P_b (days)	0.06655133843(7)
Binary orbital period derivative, $\dot{P}_b$	$1.89(5) \times 10^{-12}$
Projected semimajor axis of orbit, x (lt-s)	0.00898621(8)
Epoch of ascending node passage, T_{asc} (MJD)	56027.2483387(8)
First Laplace parameter, sin ω	$0.25(18) \times 10^{-4}$
Second Laplace parameter cos ω	$0.32(18) \times 10^{-4}$

Table 6
(Continued)

Parameter	Value
Terrestrial time standard (CLK)	TT(BIPM2011)
Reference epoch (MJD)	57551.55910304646476
Frequency of reference TOA (MHz)	1547.8940430
Solar system Ephemeris	DE436

Note. Digits in parentheses represent the 1σ uncertainty on the last quoted digit of a parameter value.

Table 7
Ephemeris of PSR J0751+1807 used in this Work and Obtained from Observations with the *NRT*

Parameter	Value
Pulsar name	J0751+1807
R.A. (J2000)	07:51:09.15481(1)
Decl. (J2000)	+18:07:38.4485(8)
Proper motion in R.A. (mas yr^{-1})	−2.65(4)
Proper motion in decl. (mas yr^{-1})	−13.0(2)
Epoch of position	56000.0
Spin frequency, ν (Hz)	287.457858396603(3)
Spin frequency derivative, $\dot{\nu}$ (s^{-2})	$6.4353(3) \times 10^{-16}$
Epoch of period	56000.0
Dispersion measure, DM (pc cm^{-3})	30.2437(2)
Dispersion measure derivative, DM1	0.0007(2)
Dispersion measure second derivative, DM2	−0.00019(3)
Epoch of DM	56000.0
Binary model	ELL1
Binary orbital period, P_b (days)	0.26314426668(3)
Binary orbital period derivative, $\dot{P}_b$	$-2.8(6) \times 10^{-14}$
Projected semimajor axis of orbit, x (lt-s)	0.3966139(4)
Rate of change of projected semimajor axis, $\dot{x}$	$-7(8) \times 10^{-16}$
Epoch of ascending node passage, T_{asc} (MJD)	51800.2157344(4)
First Laplace parameter, sin ω	$2.7(3) \times 10^{-6}$
Second Laplace parameter cos ω	$0.3(3) \times 10^{-6}$
Terrestrial time standard (CLK)	TT(BIPM2011)
Reference epoch (MJD)	57214.533388622116
Frequency of reference TOA (MHz)	1704.5
Solar system ephemeris	DE436

Note. Digits in parentheses represent the 1σ uncertainty on the last quoted digit of a parameter value.

Table 8
Ephemeris of PSR J1012+5307 used in this Work and Obtained from Observations with the *NRT*

Parameter	Value
Pulsar name	J1012+5307
R.A. (J2000)	10:12:33.438318(4)
Decl. (J2000)	+53:07:02.23033(4)
Proper motion in R.A. (mas yr^{-1})	2.665(9)
Proper motion in decl. (mas yr^{-1})	−25.50(1)
Parallax (mas)	1.0(1)
Epoch of position	56000.0
Spin frequency, ν (Hz)	190.2678373381230(3)
Spin frequency derivative, $\dot{\nu}$ (s^{-2})	$-6.20036(3) \times 10^{-16}$
Epoch of period	56000.0
Dispersion measure, DM (pc cm^{-3})	9.02169(9)
Epoch of DM	56000.0

Table 8
(Continued)

Parameter	Value
Binary model	ELL1
Binary orbital period, P_b (days)	0.604672713901(5)
Projected semimajor axis of orbit, x (lt-s)	0.58181784(4)
Epoch of ascending node passage, T_{asc} (MJD)	50700.08162698(5)
First Laplace parameter, $\sin \omega$	$1.2(1) \times 10^{-6}$
Second Laplace parameter $\cos \omega$	$0.2(1) \times 10^{-6}$
Terrestrial time standard (CLK)	TT(BIPM2011)
Reference epoch (MJD)	57211.626417018760524
Frequency of reference TOA (MHz)	1419.782959
Solar system ephemeris	DE436

Note. Digits in parentheses represent the 1σ uncertainty on the last quoted digit of a parameter value.

Table 9
Ephemeris of PSR J1552+5437 used in this Work and Obtained from Observations with *LOFAR* and *Fermi* (from Pleunis et al. 2017)

Parameter	Value
Pulsar name	J1552+5437
R.A. (J2000)	15:52:53.3311(2)
Decl. (J2000)	+54:37:05.787(1)
Epoch of position	56285
Spin frequency, ν (Hz)	411.8805314243(1)
Spin frequency derivative, $\dot{\nu}$ (s^{-2})	$-4.74(2) \times 10^{-16}$
Epoch of period	56285
Dispersion measure, DM (pc cm^{-3})	22.9000(5)
Epoch of DM	56285
Terrestrial time standard (CLK)	TT(BIPM2011)
Solar system ephemeris	DE421

Note. Digits in parentheses represent the 1σ uncertainty on the last quoted digit of a parameter value.

Table 10
Ephemeris of PSR J1744−1134 used in this Work and Obtained from Observations with the *NRT*

Parameter	Value
Pulsar name	J1744−1134
R.A. (J2000)	17:44:29.411066(1)
Decl. (J2000)	−11:34:54.72002(9)
Proper motion in R.A. (mas yr^{-1})	18.783(6)
Proper motion in decl. (mas yr^{-1})	−9.28(3)
Parallax (mas)	2.78(5)
Epoch of position	56000.0
Spin frequency, ν (Hz)	245.4261234486887(2)
Spin frequency derivative, $\dot{\nu}$ (s^{-2})	$-5.38094(2) \times 10^{-16}$
Epoch of period	56000.0
Dispersion measure, DM (pc cm^{-3})	3.13845(6)
Epoch of DM	56000.0
Terrestrial time standard (CLK)	TT(BIPM2011)
Reference epoch (MJD)	57210.939926879214401
Frequency of reference TOA (MHz)	1681.251953
Solar system ephemeris	DE436

Note. Digits in parentheses represent the 1σ uncertainty on the last quoted digit of a parameter value.

Table 11
Ephemeris of PSR J2241−5236 used in this Work and Obtained from Observations with the Parkes Radio Telescope

Parameter	Value
Pulsar name	J2241−5236
R.A. (J2000)	22:41:42.016912(2)
Decl. (J2000)	−52:36:36.21305(1)
Proper motion in R.A. (mas yr^{-1})	18.840(3)
Proper motion in decl. (mas yr^{-1})	−5.269(3)
Parallax (mas)	0.83(3)
Epoch of position	55044.15587
Spin frequency, ν (Hz)	457.3101568473538(3)
Spin frequency derivative, $\dot{\nu}$ (s^{-2})	$-1.442288(2) \times 10^{-15}$
Epoch of period	55044.15587
Dispersion measure, DM (pc cm^{-3})	11.44(1)
Epoch of DM	55044.15587
Binary model	ELL1
Binary orbital period, P_b (days)	0.145672237818(2)
Time derivative of orbital frequency (Hz s^{-1})	$-3.17(3) \times 10^{-21}$
Projected semimajor axis of orbit, x (lt-s)	0.02579536(1)
Rate of change of projected semimajor axis	$1.3(1) \times 10^{-15}$
Epoch of ascending node passage, T_{asc} (MJD)	56726.96359375(1)
First Laplace parameter, $\sin \omega$	$3(8) \times 10^{-7}$
Second Laplace parameter $\cos \omega$	$7(8) \times 10^{-7}$
Terrestrial time standard (CLK)	TT(TAI)
Reference epoch (MJD)	57831.06107389881430
Solar system ephemeris	DE421

Note. Digits in parentheses represent the 1σ uncertainty on the last quoted digit of a parameter value.

ORCID iDs

Sebastien Guillot ⓘ https://orcid.org/0000-0002-6449-106X
Matthew Kerr ⓘ https://orcid.org/0000-0002-0893-4073
Paul S. Ray ⓘ https://orcid.org/0000-0002-5297-5278
Slavko Bogdanov ⓘ https://orcid.org/0000-0002-9870-2742
Scott Ransom ⓘ https://orcid.org/0000-0001-5799-9714
Julia S. Deneva ⓘ https://orcid.org/0000-0003-1226-0793
Deepto Chakrabarty ⓘ https://orcid.org/0000-0001-8804-8946
Wynn C. G. Ho ⓘ https://orcid.org/0000-0002-6089-6836
Gaurava K. Jaisawal ⓘ https://orcid.org/0000-0002-6789-2723
Christian Malacaria ⓘ https://orcid.org/0000-0002-0380-0041
M. Coleman Miller ⓘ https://orcid.org/0000-0002-2666-728X
Tod E. Strohmayer ⓘ https://orcid.org/0000-0001-7681-5845
Michael T. Wolff ⓘ https://orcid.org/0000-0002-4013-5650
Lucas Guillemot ⓘ https://orcid.org/0000-0002-9049-8716

References

Abbott, B. P., Abbott, R., Abbott, T. D., et al. 2018, PhRvL, 121, 161101
Abbott, B. P., Abbott, R., Abbott, T. D., et al. 2017, PhRvL, 119, 161101
Alpar, M. A., Cheng, A. F., Ruderman, M. A., & Shaham, J. 1982, Natur, 300, 728
Antoniadis, J., Tauris, T. M., Ozel, F., et al. 2016, arXiv:1605.01665
Arzoumanian, Z., Brazier, A., Burke-Spolaor, S., et al. 2018, ApJS, 235, 37
Astropy Collaboration, Price-Whelan, A. M., Sipőcz, B. M., et al. 2018, AJ, 156, 123
Baillot d'Etivaux, N., Guillot, S., Margueron, J., et al. 2019, arXiv:1905.01081
Bassa, C. G., Janssen, G. H., Stappers, B. W., et al. 2016, MNRAS, 460, 2207

Becker, W., & Aschenbach, B. 2002, in Proc. 270 WE-Heraeus Seminar, Neutron Stars Pulsars, and Supernova Remnants, ed. W. Becker, H. Lesch, & J. Trümper (Garching: Max-Plank-Institut für extraterrestrische Physik), 64

Becker, W., & Trümper, J. 1993, Natur, 365, 528

Becker, W., & Trümper, J. 1999, A&A, 341, 803

Beronya, D. M., Karpova, A. V., Kirichenko, A. Y., et al. 2019, MNRAS, 485, 3715

Bilous, A. V., Watts, A. L., Harding, A. K., et al. 2019, ApJL, L23

Bisnovatyi-Kogan, G. S., & Komberg, B. V. 1974, SvA, 18, 217

Blandford, R., & Teukolsky, S. A. 1976, ApJ, 205, 580

Bogdanov, S. 2013, ApJ, 762, 96

Bogdanov, S., & Grindlay, J. E. 2009, ApJ, 703, 1557

Bogdanov, S., Grindlay, J. E., Heinke, C. O., et al. 2006, ApJ, 646, 1104

Bogdanov, S., Grindlay, J. E., & Rybicki, G. B. 2008, ApJ, 689, 407

Bogdanov, S., Guillot, S., Ray, P., et al. 2019, ApJL, L25

Bogdanov, S., Heinke, C. O., Özel, F., & Güver, T. 2016, ApJ, 831, 184

Bogdanov, S., Rybicki, G. B., & Grindlay, J. E. 2007, ApJ, 670, 668

Bogdanov, S., van den Berg, M., Servillat, M., et al. 2011, ApJ, 730, 81

Callanan, P. J., Garnavich, P. M., & Koester, D. 1998, MNRAS, 298, 207

Cameron, P. B., Rutledge, R. E., Camilo, F., et al. 2007, ApJ, 660, 587

Chen, H.-L., Chen, X., Tauris, T. M., & Han, Z. 2013, ApJ, 775, 27

Crawford, F., Roberts, M. S. E., Hessels, J. W. T., et al. 2006, ApJ, 652, 1499

Cromartie, H. T., Fonseca, E., Ransom, S. M., et al. 2019, NatAs, in press

de Jager, O. C., & Büsching, I. 2010, A&A, 517, L9

de Jager, O. C., Raubenheimer, B. C., & Swanepoel, J. W. H. 1989, A&A, 221, 180

De, S., Finstad, D., Lattimer, J. M., et al. 2018, PhRvL, 121, 091102

Deneva, J. S., Ray, P. S., Lommen, A., et al. 2019, ApJ, 874, 160

Desvignes, G., Caballero, R. N., Lentati, L., et al. 2016, MNRAS, 458, 3341

Draghis, P., & Romani, R. W. 2018, ApJ, 862, L6

Fonseca, E., Pennucci, T. T., Ellis, J. A., et al. 2016, ApJ, 832, 167

Forestell, L. M., Heinke, C. O., Cohn, H. N., et al. 2014, MNRAS, 441, 757

Freire, P. C. C., & Tauris, T. M. 2014, MNRAS, 438, L86

Gendreau, K., & Arzoumanian, Z. 2017, NatAs, 1, 895

Gentile, P. A., Roberts, M. S. E., McLaughlin, M. A., et al. 2014, ApJ, 783, 69

Gotthelf, E. V., & Bogdanov, S. 2017, ApJ, 845, 159

Guillemot, L., Smith, D. A., Laffon, H., et al. 2016, A&A, 587, A109

Guillot, S. 2016, MmSAI, 87, 521

Guillot, S., Servillat, M., Webb, N. A., & Rutledge, R. E. 2013, ApJ, 772, 7

Harding, A. K., & Muslimov, A. G. 2001, ApJ, 556, 987

Harding, A. K., & Muslimov, A. G. 2002, ApJ, 568, 862

Heinke, C. O., Cohn, H. N., Lugger, P. M., et al. 2014, MNRAS, 444, 443

Heinke, C. O., Rybicki, G. B., Narayan, R., & Grindlay, J. E. 2006, ApJ, 644, 1090

Hessels, J., Ransom, S., Roberts, M., et al. 2005, in ASP Conf. Ser. 328, Binary Radio Pulsars, ed. F. A. Rasio & I. H. Stairs (San Francisco, CA: ASP), 395

Hessels, J. W. T., Ransom, S. M., Stairs, I. H., et al. 2006, Sci, 311, 1901

HI4PI Collaboration, Ben Bekhti, N., Flöer, L., et al. 2016, A&A, 594, A116

Hibschman, J. A., & Arons, J. 2001, ApJ, 554, 624

Hobbs, G., & Edwards, R. 2012, TEMPO2: Pulsar Timing Package, Astrophysics Source Code Library, ascl:1210.015

Hobbs, G. B., Edwards, R. T., & Manchester, R. N. 2006, MNRAS, 369, 655

Hotan, A. W., van Straten, W., & Manchester, R. N. 2004, PASA, 21, 302

Kaplan, D. L., Kupfer, T., Nice, D. J., et al. 2016, ApJ, 826, 86

Kargaltsev, O., Durant, M., Pavlov, G. G., & Garmire, G. 2012, ApJS, 201, 37

Keith, M. J., Johnston, S., Ray, P. S., et al. 2011, MNRAS, 414, 1292

Kerr, M., Coles, W. A., Ward, C. A., et al. 2018, MNRAS, 474, 4637

Kramer, M., Lange, C., Lorimer, D. R., et al. 1999, ApJ, 526, 957

Lattimer, J. M., & Prakash, M. 2016, PhR, 621, 127

Lee, J., Hui, C. Y., Takata, J., et al. 2018, ApJ, 864, 23

Lundgren, S. C., Zepka, A. F., & Cordes, J. M. 1995, ApJ, 453, 419

Luo, J., Ransom, S., Demorest, P., et al. 2019, PINT: High-precision pulsar timing analysis package, Astrophysics Source Code Library, ascl:1902.007

Lynch, R. S., Swiggum, J. K., Kondratiev, V. I., et al. 2018, ApJ, 859, 93

Lyne, A. G., & Manchester, R. N. 1988, MNRAS, 234, 477

Manchester, R. N., Lyne, A. G., D'Amico, N., et al. 1996, MNRAS, 279, 1235

Marelli, M., De Luca, A., & Caraveo, P. A. 2011, ApJ, 733, 82

Miller, M. C. 2013, arXiv:1312.0029

Miller, M. C. 2016, ApJ, 822, 27

Miller, M. C., Chirenti, C., & Lamb, F. K. 2019, arXiv:1904.08907

Miller, M. C., & Lamb, F. K. 2015, ApJ, 808, 31

Mingarelli, C. M. F., Anderson, L., Bedell, M., & Spergel, D. N. 2018, arXiv:1812.06262

Nandra, K., Barret, D., Barcons, X., et al. 2013, arXiv:1306.2307

Nasa High Energy Astrophysics Science Archive Research Center (Heasarc) 2014, HEAsoft: Unified Release of FTOOLS and XANADU, Astrophysics Source Code Library, ascl:1408.004

Nicastro, L., Lyne, A. G., Lorimer, D. R., et al. 1995, MNRAS, 273, L68

Nice, D. J., Splaver, E. M., Stairs, I. H., et al. 2005, ApJ, 634, 1242

Özel, F., Baym, G., & Güver, T. 2010, PhRvD, 82, 101301

Özel, F., Psaltis, D., Güver, T., et al. 2016, ApJ, 820, 28

Pancrazi, B., Webb, N. A., Becker, W., et al. 2012, A&A, 544, A108

Papitto, A., Ferrigno, C., Bozzo, E., et al. 2013, Natur, 501, 517

Parent, E., Kaspi, V. M., Ransom, S. M., et al. 2019, arXiv:1908.09926

Pavlov, G. G., Kargaltsev, O., Garmire, G. P., & Wolszczan, A. 2007, ApJ, 664, 1072

Pavlov, G. G., & Zavlin, V. E. 1997, ApJL, 490, L91

Pleunis, Z., Bassa, C. G., Hessels, J. W. T., et al. 2017, ApJL, 846, L19

Predehl, P., Andritschke, R., Becker, W., et al. 2014, Proc. SPIE, 9144, 91441T

Radhakrishnan, V., & Srinivasan, G. 1982, CSci, 51, 1096

Ransom, S. M., Ray, P. S., Camilo, F., et al. 2011, ApJL, 727, L16

Ray, P. S., Arzoumanian, Z., Ballantyne, D., et al. 2019a, arXiv:1903.03035

Ray, P. S., Arzoumanian, Z., & Gendreau, K. C. 2018, in IAU Symp. 337, Pulsar Astrophysics the Next Fifty Years, NICER Working Group on Pulsation Searches and Multiwavelength Coordination, ed. P. Weltevrede (Cambridge: Cambridge Univ. Press), 187

Ray, P. S., Guillot, S., Ransom, S. M., et al. 2019b, ApJL, 878, L22

Reardon, D. J., Hobbs, G., Coles, W., et al. 2016, MNRAS, 455, 1751

Riley, T. E., Watts, A. L., Bogdanov, S., et al. 2019, ApJL, L21

Rosen, S. R., Webb, N. A., Watson, M. G., et al. 2016, A&A, 590, A1

Shklovskii, I. S. 1970, AZh, 47, 742

Spiewak, R., Kaplan, D. L., Archibald, A., et al. 2016, ApJ, 822, 37

Steiner, A. W., Heinke, C. O., Bogdanov, S., et al. 2018, MNRAS, 476, 421

Steiner, A. W., Lattimer, J. M., & Brown, E. F. 2010, ApJ, 722, 33

Steiner, A. W., Lattimer, J. M., & Brown, E. F. 2013, ApJL, 765, L5

Stovall, K., Lynch, R. S., Ransom, S. M., et al. 2014, ApJ, 791, 67

Sturrock, P. A. 1971, ApJL, 169, L7

Sutaria, F. K., Ray, A., Reisenegger, A., et al. 2003, A&A, 406, 245

Swiggum, J. K., Kaplan, D. L., McLaughlin, M. A., et al. 2017, ApJ, 847, 25

Testa, V., Mignani, R. P., Pallanca, C., Corongiu, A., & Ferraro, F. R. 2015, MNRAS, 453, 4159

van Haarlem, M. P., Wise, M. W., Gunst, M. W., et al. 2013, A&A, 556, A2

van Kerkwijk, M. H., Bergeron, P., & Kulkarni, S. R. 1996, ApJL, 467, L89

Watts, A. L., Yu, W., Poutanen, J., et al. 2019, SCPMA, 62, 29503

Webb, N. A., & Barret, D. 2007, ApJ, 671, 727

Webb, N. A., Leahy, D., Guillot, S., et al. 2019, A&A, 627, A141

Webb, N. A., Olive, J. F., & Barret, D. 2004a, A&A, 417, 181

Webb, N. A., Olive, J.-F., Barret, D., et al. 2004b, A&A, 419, 269

Wijnands, R., & van der Klis, M. 1998, Natur, 394, 344

Yao, J. M., Manchester, R. N., & Wang, N. 2017, ApJ, 835, 29

Zavlin, V. E. 2006, ApJ, 638, 951

Zavlin, V. E., Pavlov, G. G., Sanwal, D., et al. 2002, ApJ, 569, 894

Zavlin, V. E., Pavlov, G. G., & Shibanov, Y. A. 1996, A&A, 315, 141